Large scale response of a vehicle wake to on-road perturbations

Agostino Cembalo, Jacques Borée, Patrick Coirault, Clément Dumand

Large scale response of a vehicle wake to on-road perturbations

Agostino Cembalo[a,c], Jacques Borée[a,*], Patrick Coirault[b], Clément Dumand[c]

[a] *Pprime Institute CNRS, ENSMA, University of Poitiers, 1 Av. Clément Ader, 86360, Chasseneuil-du-Poitou, France*
[b] *Laboratory LIAS - ENSIP, University of Poitiers, 2 rue Pierre Brousse, 86073, Poitiers, France*
[c] *STELLANTIS, Advanced Innovation, 212 Bd Pelletier, Carrières-sous-Poissy, 78955, France*

Abstract

Under disturbed upstream conditions, numerous wind tunnel studies have shown that the near wake region of a vehicle loses its average symmetry, resulting in an increase of drag. The aim of this research work is to analyse the large scale response of a vehicle wake to on-road perturbations by using an instrumented vehicle and by comparing scale one wind tunnel tests, track trials and on road experiments. More precisely, in all these tests, we focus on the analysis of the asymmetry of the pressure distribution at the base. Proper Orthogonal Decomposition (POD) is used. For all cases considered, POD analysis reveals two dominant modes, respectively associated with vertical and horizontal wake large scale reorganisation. More than 50% of the total energy is carried by these two modes and this value increases significantly for on-road tests. Noteworthy, the low-frequency energy content of the temporal coefficients of these modes is significantly higher on-road. Low frequencies (even very low ones) then play a major role, corresponding to a quasi-static perturbation domain of the velocity seen by the vehicle. We show that a quasi-steady exploration of the on-road yaw angle statistical distribution during a wind tunnel test captures phenomena similar to those observed on the road and is therefore interesting to evaluate on-road aerodynamic performances. This also opens perspectives for developing closed loop control strategies aiming to maintain a prescribed wake balance in order to reduce drag experienced on the road.

Keywords: Automotive aerodynamics, Drag Reduction, Wind Tunnel tests, On-Road tests

1. Introduction

The European Environment Agency has assessed the impact of transports on greenhouse gases and state that "*Transport is responsible for a quarter of the EU's greenhouse gas emissions, with road transport representing the greatest share (72% in 2019).*" [1] Moreover, it is estimated that passenger cars are still the dominant transportation mean with a share of approximately 80% [2]. These studies highlight the importance of reducing the greenhouse gases emissions of road transportation and in this regards vehicle aerodynamics plays a crucial role. In fact, at highway speeds, approximately 70% of the energy losses can be attributed to aerodynamic forces (Kadijk and Ligterink [1], Hucho and Sovran [2]). In that respect, vehicle manufacturers put a lot of effort in optimizing vehicle's aerodynamics both with numerical simulations and wind tunnel testing. However, the vehicle's surroundings are constantly changing in real-life scenarios (Cooper [3], Watkins et al. [4]) and the drag coefficient, usually optimised at zero yaw condition, varies continuously.

As yaw angle is concerned, several studies have assessed an on-road average yaw angle distribution (Carlino et al. [5], de la Cruz et al. [6], Yamashita et al. [7], Stoll and Wiedemann [8]), showing that, on average, this distribution corresponds to a quasi-normal distribution centered around 0° with a standard deviation varying upon the external perturbations of the velocity seen by the vehicle due not only to wind turbulence but also to varying road surroundings such as guardrails, vehicles, bushes and trees among others. Hence, only considering the zero yaw angle drag coefficient translates into an under-prediction of the actual averaged drag coefficient. Howell et al. [9] have addressed this problem by defining a wind averaged drag coefficient, on a WLTP (Worldwide Harmonised Light vehicles Test Procedure [10]) road cycle, using quasi-steady approaches :

$$C_{DWC} = 0.530C_{D0} + 0.345C_{D5} + 0.130C_{D10} + 0.007C_{D15},$$

C_{Di} $(i = 0, 5, 10, 15°)$ being the drag coefficient at a given yaw angle and C_{DWC} being the averaged drag coefficient based on a typical wind distribution. This wind averaged drag coefficient is larger than its value at zero yaw. The authors of this study therefore specifically highlight the importance of reducing the sensitivity of the aerodynamic loads to the on-road perturbations. Route-specific wind simulations were proposed for heavy duty vehicles byMcTavish and McAuliffe [11]. Although not considered in this

*Corresponding author

[1] https://www.eea.europa.eu//publications/transport-and-environment-report-2021

[2] https://www.eea.europa.eu/publications/transport-and-environment-report-2022/transport-and-environment-report/view

study, it is also now well known that aerodynamic drag in cycling is highly sensitive to external turbulence (Brown et al. [12]).

Cooper and Watkins [13] and Watkins and Cooper [14] successfully measured the unsteady flow characteristics seen by a road vehicle. They showed that the mean turbulence intensity is of the order of 5% with integral length scales of the order of tens of meters. Moreover, turbulence seen by the vehicle has a rich spectra (Hu et al. [15], Su et al. [16]) over a wide range of frequencies and it has been found that the wind gusts feed the spectrum in the low frequencies. Similar results have been found by Wordley and Saunders [17], Wordley and Saunders [18] and Schröck et al. [19]. The first two studies focus on the effect of four different terrain variations on the turbulence scales and intensities. It is shown that "*the four different terrain overlap in the region of lower turbulence intensity ($< 5\%$) and smaller turbulent length scale ($< 5\ m$)*". The study of (Schröck et al. [19]) emphasizes that, when the wind intensity grows, the energy content of the turbulence spectrum seen by the vehicle shifts to the low frequency region, resulting in about 75% of the energy content at frequencies below 2 Hz.

Although not detailed here for the sake of brevity, a number of wind tunnel or CFD studies (Bonnavion et al. [20], Rüttgers et al. [21], Burton et al. [22]) have demonstrated that an important source of increased pressure drag under varying upstream flow conditions is the large scale separated near-wake region at the rear of the vehicle. Under disturbed upstream conditions, this near-wake region loses its average symmetry, resulting in an increase in drag. If the deviation from the reference situation is small, these asymmetries in the vicinity of the wake can be compensated for. Passive or active actuation can be designed to impart local flow deviation by means of tapers or flaps (a strategy called 'pressure control') or by modifying the turbulent characteristics of the unsteady shear layer surrounding the near wake (a strategy called 'turbulence control'). Such strategies have been demonstrated in steady-state situations. For example, for small yaw angles representative of actual driving conditions, in steady-state situations, mechanical flaps (Urquhart and Sebben [23], Urquhart et al. [24]), asymmetric tapers (Perry et al. [25], Varney et al. [26]), or high-frequency pulsed jets (Li et al. [27]) counteract yaw-induced asymmetry of the near-wake recirculation region, leading to reduced drag. As proposed by (Varney et al. [26]) for asymmetric tapering, *"Applying this approach to configure an adaptive system on a vehicle could have real benefit in terms of drag reduction with the ability to adapt to any given real-world yaw condition, along with the potential to improve cross wind stability"*. With this perspective in mind, a quasi-steady closed loop control able to maintain a prescribed wake balance on a 2/5 reduced scale Windsor model was recently proposed by Cembalo et al. [28] using recursive subspace-based predictive control.

As an important follow-up on all these contributions, our objective in this paper is to provide data and to analyze the spatio-temporal distribution of the static pressure at the base of a vehicle submitted to on-road perturbations with two major questions. First, in order to determine if the external perturbations seen by the vehicle result in significant vertical or horizontal large-scale asymmetries of the wake that we expect to contribute significantly to the mean drag experienced by the vehicle. Second, in order to see if low frequency global wake motions have a major contribution in real situations. Indeed, it will then be interesting to search for quasi-steady active control solution because the time scale of the external forcing of the wake by the slow external perturbations is much larger than the advective time scale driving unsteady aerodynamic responses.

To achieve this objective, we equipped a vehicle with a Prandtl antenna and a Conrad probe at the front as well as 49 pressure taps at the base. The vehicle was tested in a wind tunnel and driven on a track and on the road. Through the collected data, we analyze in this paper the pressure asymmetry of the wake and compare the results between wind tunnel experiments and road testing.

The paper is organised as follows: Section 2 describes the wind tunnel used and on-road routes. Section 3 provides details on the instrumentation of the vehicle and data processing methodology. In Section 4 we focus on the wind tunnel experiments at zero yaw angle. Section 5 highlights the main results obtained on-road and some comparison with the wind tunnel results are made. Section 6 provides a statistical comparison between the on-road tests and a test with a dynamically varying yaw angle in the wind tunnel. Concluding remarks are proposed in Section 7.

2. Presentation of wind tunnel and on-road routes

For this study, we were able to make use of the Stellantis wind tunnel located in Orbassano (10043, Italy) (Stellato and Betti [29]), the Stellantis track of La Ferté-Vidame (28340, France) and a RDE-like route (Yvelines, 78000, France), which are shown in the Figures 1 and 2 respectively.

Stellantis Wind Tunnel

From the control room (1), operators can activate the wind tunnel. The test section (2) is 3/4 open, with a variable nozzle section ranging from $22\,\mathrm{m}^2$ to $30.5\,\mathrm{m}^2$ in a plenum measuring 10.5 meters long, 12.2 meters wide, and 10.8 meters high. The turbulence rate at the center of the section is less than 0.5%, and the boundary layer, at $X = 2.5\,\mathrm{m}$ from the exit of the convergent, has a thickness of 5 mm with the boundary layer suction function activated. The maximum test speed is $U_\infty = 215\,\mathrm{km/h}$ with a system of 5 moving belts, one under the car and the remaining four under the wheels to allow their rotation. The test speed for our tests is constant at $U_\infty = 110\,\mathrm{km/h}$. The car is positioned on a turntable (3) measuring 7 meters in

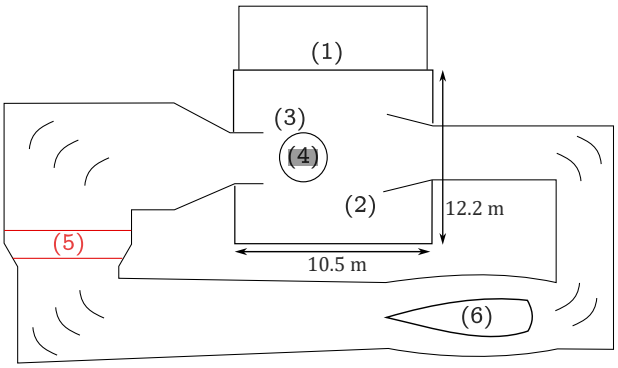

Figure 1: Sketch of the Stellantis wind tunnel in Orbassano (10043, Italy).

diameter. Beneath the turntable, a six-component balance (4) is installed to measure aerodynamic forces. The vehicle is attached to the balance using four masts, with which we can also adjust the vehicle's ground clearance, set to the same value as measured with two people inside the vehicle for road tests. Through the heat exchanger (5), we control the temperature to remain constant at $T = 22°\mathrm{C}$ throughout the tests. The wind is set in motion with a motor-driven fan (6).

On-road routes

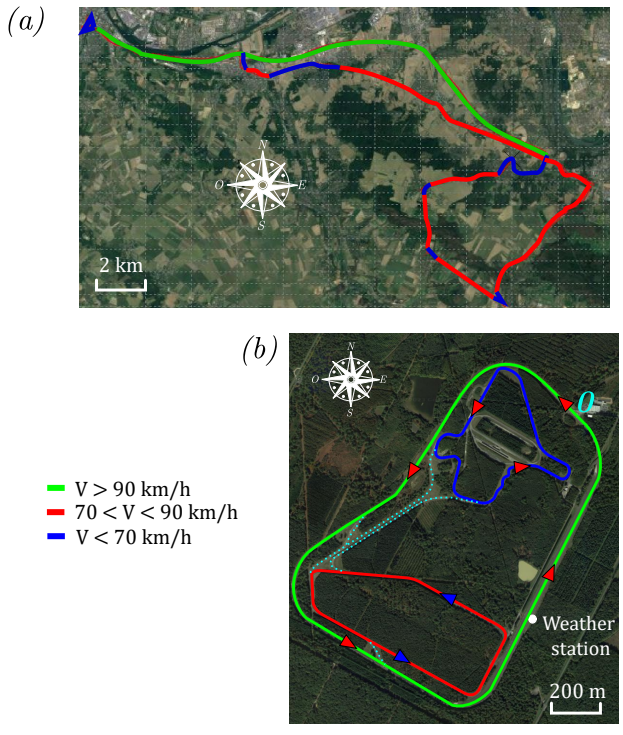

Figure 2: On-road routes. (a) RDE-like route in the Yvelines (78000, France). (b) Stellantis track of La Ferté-Vidame (28340, France).

The "RDE-like" route (RDE: Real Driving Emissions) (part (a) of the Figure 2) is a route that partially fullfils to the kilometer distribution in accordance with the new regulatory guidelines for the vehicle homologation process (WLTP [10]). It measures approximately 68 kilometers. The whole route allows, most of the time, vehicle speed above 70 km/h for which aerodynamic efficiency becomes predominant when compared to the rolling resistance of the vehicle. The kilometer distribution contains approximately 43% of highway, 46% of rural roads and 11% of urban area. Using the Eurocode 1 norm of wind engineering (see for example [30] and [31]), approximately 70% of the terrains surrounding the route are of category IIIa, corresponding to countryside with hedgerows, hedged farmland and scattered settlements. The remaining route is of category IIIb ($\sim 20\%$), corresponding to urbanised or industrial areas or dense hedged farmland and of category IV ($\sim 10\%$) with woods. The corresponding surface roughness parameter $z_0(m)$ and minimun height $z_{min}(m)$ for these categories IIIa, IIIb and IV are respectively $(z_0, z_{min}) = (0.2, 5); (0.5, 9); (1, 15)$. Corresponding turbulent intensities are considered constant for heights lower than z_{min} and can be obtained from the norm. However, as stated by Wordley and Saunders [17], Cooper and Watkins [13], the last few meters close to the ground where vehicles are driven are still not well understood. Atmospheric pressure information as well as wind speed and orientation were obtained from averages of several weather stations in the area.

Tests were also conducted at the Stellantis site in La Ferté-Vidame (28340, France) (Figure 2b). This site consists of three tracks: the Outer Track (in green), the Bel Air Track (in red), and the Park Track (in blue). The colors correspond to the permitted speeds on the tracks, so the Outer Track corresponds to a highway route, the Bel Air Track corresponds to a rural route, and the Park Track corresponds to an urban route. We mainly conducted tests on the Outer Track and the Bel Air Track. The Outer Track measures approximately $\sim 6.5\ km$ and includes four main turns. This track allows for a speed constantly over 90 km/h throughout the test. The Bel Air Track measures approximately $\sim 3.3\ km$ and includes several short-radius turns, allowing for a speed of $70\ km/h \leq V \leq 90\ km/h$. These tracks are connected by connecting ramps (sky-blue dashed lines). The La Ferté-Vidame site has a weather station capable of measuring wind speed and direction, as well as temperature and atmospheric pressure. A closer look at Figure 2b shows that the tracks are surrounded by woods. Using Eurocode 1 norm ([30] and [31]), the terrain surrounding the site is of category IV. All tests conducted on the tracks start at point 0 (in sky-blue), which corresponds to the main entrance of the tracks. The direction of travel is indicated by red triangles. However, each day, the direction of travel is reversed to be able to conduct tests in both directions and ensure that the cars and the track degrade uniformly and not biased by the direction of travel. In our tests, the number of people in the vehicle is always two. There is a driver and the person responsible for verifying the correct progress of the acquisition. The

passenger sits in the rear seat where a PC mounting system has been installed to ensure safety requirements. A zero calibration is performed before each test to compensate for any pressure signal drift that may be present. This calibration is performed in a closed building to prevent small disturbances from affecting the process. Acquisition is initiated just before starting the test and stopped once the vehicle is stationary again.

3. Instrumentation of the vehicle and data processing methodology

A Citroën C4 Cactus, shown in Figure 3, has been used. The vehicle is equipped with a Prandtl antenna, a Conrad probe, a GPS system and 49 pressure taps at the base.

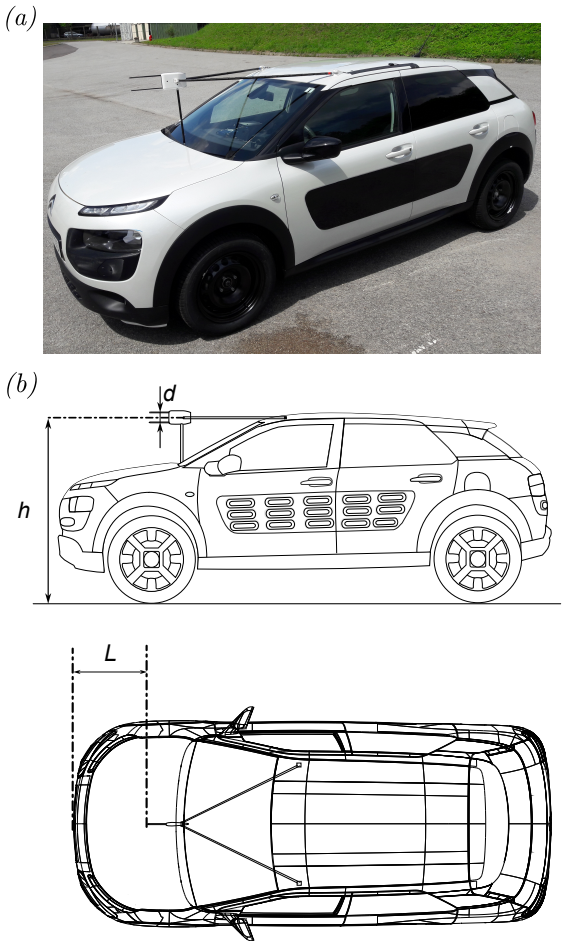

Figure 3: Testing vehicle (Citröen C4 Cactus). (a) Real front-side view of the vehicle. (b) Drawings of the side and top view with characteristic dimensions. d = 80mm, h = 1450mm and L = 745mm.

Both Prandtl and Conrad probes have been constructed internally in a Stellantis' workshop, mainly following the instructions detailed in Chue [32]. They have been calibrated and tested by Thomann [33]. The Prandtl antenna grants an angular tolerance of $\pm 10°$ while the Conrad probe has a maximum sensitivity of 60° with a linear

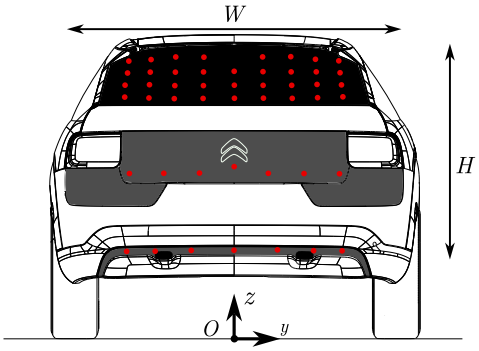

Figure 4: Position of the 49 pressure taps on the vehicle's base. O is the origin of the coordinate system. $W = 1150mm$ and $H = 900mm$ are respectively the width and height of the base.

trend for $-15° \leq \beta \leq 15°$. Both Prandtl antenna and Conrad probe are located in the car's center-line plane (Figure 3) and were carefully aligned using a laser sheet. The distance d between the two probes is $d = 80mm$ and the Prandtl antenna is located above. The distance L of probe tips from the front of the car is $L = 745mm$. The height h of the mid-plane between the probe is equal to $h = 1450mm$. The probes are respectively linked with a *Texxis DPS 50 - 0.5* and a *Texxis DPS 50 - 2.5* differential pressure scanners. The signals are sent to a *VBOX Racelogic* which includes the GPS system.

A differential pressure scanner *Scanivalve MPS4264* is mounted in the trunk of the car. The 64 pressure ports have a range of 8" H_2O. Since it is a differential pressure scanner, this means that the pressure p_i measured on the i_{th} tap is given by $p_i = p_{a_i} - p_r$, where p_{a_i} is the absolute pressure on the i_{th} tap and p_r is the reference pressure. In our specific case, the reference pressure is obtained using a pierced aluminum bottle mounted inside the trunk of the car. This allows to always refer to the static pressure in the trunk of the car while minimising the pressure fluctuations by acting like a low-pass filter. The position of the pressure taps at the base of the car is shown in Figure 4. The length of the vinyl tubes connected to the scanner varies considerably. At the base, this length can range from 0.7 meters to 2.6 meters, depending on the pressure tap considered. For each measurement channel and therefore each tube length, a phase and amplitude correction was carried out by convolution with a specifically determined transfer function (see Gravier [34]). To find out the transfer function, the method proposed by Tijdeman and Bergh [35] was used taking into account the geometric properties of the circuit for each channel. In order to properly validate some sensitive information from the physical model derived by these authors, such as for example the radius of the vinyl tubes, a calibration was carried out on a specific test bench for several lengths. The calibration bench also made it possible to verify that, over the frequency range considered here ($f < 20Hz$) and after correction, the phase and module of the signals are accurately corrected.

The acquired pressure data is then post-processed to

calculate the pressure coefficient:

$$C_{p_i} = \frac{p_i - p_r}{Q}, \tag{1}$$

where p_i represents the pressure measured at the i_{th} pressure tap, p_r is the reference pressure in the vehicle trunk, and $Q = \frac{1}{2}\rho_\infty U_\infty^2$ is the dynamic pressure, with ρ_∞ as the air density and U_∞ as the free-stream velocity. During on road tests, U_∞ is the velocity deduced by the GPS system at the time of the measurement.

The following notation will be used for spatial ($\langle A \rangle$) and temporal ($\overline{A}$) averaging, respectively:

$$\langle A \rangle(t_m) = \frac{1}{N}\sum_{n=1}^{N} A(\mathbf{x}_n, t_m),$$

$$\overline{A}(x_n) = \frac{1}{M}\sum_{m=1}^{M} A(\mathbf{x}_n, t_m),$$

where N and M are the number of pressure taps at the base and the number of time steps, respectively.

However, it is necessary to note that measuring the reference pressure on-road remains a very complicated task because the slightest variation in the vehicle results in a variation in the pressure. Comparisons between the speed data obtained using the Prandtl antenna and those obtained using tachymetric measurements have shown that the reference pressure is not constant. The instantaneous difference between the pressure coefficient of each sensor and the spatial average of the pressure coefficient at the base at the same instant is defined as :

$$C_p^*(\mathbf{x}_n, t_m) = C_p(\mathbf{x}_n, t_m) - \langle C_p(t_m) \rangle. \tag{2}$$

Hereafter, we will always use $C_p^*(x_n, t_m)$ in order to eliminate any temporal variation in the reference pressure during a test. By using $C_p^*(x_n, t_m)$, we therefore focus on the asymmetry of the wake corresponding to the deviation from the spatial average of the instantaneous pressure distribution at the base.

The main objective of the measurement sessions is to characterize the wake of the car in terms of global motions and to analyse the frequency of these motions. Proper Orthogonal Decomposition (POD) will be used in that respect. This analysis method was first introduced by Lumley [36] with the aim of decomposing the flow's turbulence into deterministic functions, each of which can capture a portion of the flow's turbulent kinetic energy. Several works have summarized this method and explained how to use it (Chatterjee [37], Cordier and Bergmann [38], Taira et al. [39], Weiss [40]).

In our specific case, the principle of POD, calculated here by the direct method after substracting the time average of $\overline{C_p^*(\mathbf{x}_i, t)}$, consists of decomposing the vector $C_p^*(\mathbf{x}_i, t)$ into a set of deterministic functions $\Phi^{(k)}(\mathbf{x})$ that are modulated by N temporal coefficients $a^{(k)}(t)$ as follows:

$$C_p^*(\mathbf{x}_i, t) = \overline{C_p^*(\mathbf{x}_i, t)} + \sum_{k=1}^{N_{modes}} a^{(k)}(t)\Phi^{(k)}(\mathbf{x}_i). \tag{3}$$

It is important to recall that the functions $\Phi^{(k)}$ are orthogonal.

The decomposition is performed using singular value decomposition, that provides the functions $\Phi^{(k)}$, which we will call modes hereafter, as well as the eigenvector $\boldsymbol{\lambda}$, which contains the contribution of each mode, in decreasing order, to the total variance. In our study, the number of modes corresponds to the number of pressure sensors at the base, which is 49 modes in total. This means that we have a signal decomposition in the form:

$$C_p^*(\mathbf{x}_i, t) = \overline{C_p^*(\mathbf{x}_i, t)} + \sum_{k=1}^{49} a^{(k)}(t)\Phi^{(k)}(\mathbf{x}_i),$$

with the total energy defined as follows:

$$\xi = \sum_{i=1}^{N_{taps}} \overline{{C_{p_i}^*}^2} = \sum_{k=1}^{N_{modes}} \lambda_k.$$

Additionally, thanks to the temporal coefficients of the modes ($a^{(k)}(t)$), it is possible to analyze the frequency characteristics of the projection of the velocity field onto each mode.

In what follows, we will concentrate on the two first POD modes because they contain a significant contribution of the total variance. We remind that, by using $C_p^*(\mathbf{x}, t)$, we focus on the asymmetry of the wake.

4. Wind tunnel testing

We consider here a case with zero yaw angle ($\beta = 0°$). The results are presented in Figure 5.
The distribution of β shown in the Figure (top-left panel) has a mean $\mu_\beta = -0.3°$ and a standard deviation $\sigma_\beta = 0.13°$. It is not centered at $\beta = 0°$ due to some slight human errors, such as alignment to the symmetry plane of the wind tunnel and alignment of the Conrad probe to the vehicle's symmetry plane. The latter error remains constant throughout our tests. This distribution of β corresponds to typical cases analyzed by automotive manufacturers, i.e., a nearly constant yaw angle throughout the test. Under these conditions, we performed the POD analysis. The energy contribution of the 49 modes is presented in the bottom-left panel of the figure. We can observe that the first two modes contribute significantly to the total wake energy (approximately 45%), so we will analyze these two modes, which are presented in the top-right panel of the figure. It is interesting to note that these modes have well-defined footprints. For the first mode, we can associate this footprint with a vertical tilting of the wake.

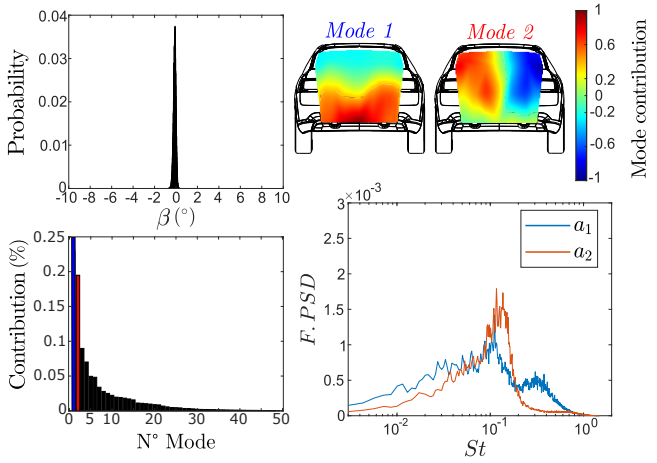

Figure 5: Results of the wake analysis for a fixed zero yaw angle in the wind tunnel. Presentation of the distribution of β, the first two modes, the percentage of their contribution to the total energy, as well as spectral analysis of the temporal coefficients associated with the two modes.

In contrast, the footprint of the second mode reveals a horizontal tilting. For this configuration, it is relevant to analyze the characteristic frequencies of these two asymmetries. To do this, we calculated the spectra of the two corresponding temporal coefficients with a frequency resolution $\Delta f = 5.10^{-2}\ Hz$. This frequency resolution corresponds to a division of the signal into 53 blocks, which will be the minimum number of blocks used subsequently. In the bottom-right panel of the figure, a pre-multiplied spectrum is presented showing the spectra of the two temporal coefficients. Regarding the frequencies, we chose to represent dimensionless frequencies to compare the different tests performed. For this purpose, we used the Strouhal number ($St = f.H/V$), which is the product of the frequency and the advective time scale (H/V). Note that the frequency range $f < 20\ Hz$ corresponds here to a Strouhal number of $St < 0.6$, which means that phases and amplitudes are accurately corrected for all taps in the relevant frequency range. Moreover, from measurements performed with reduced scale models in a wind tunnel (Haffner et al. [41]) we do not expect significant higher frequency contributions for large scale events. We observe a large band distribution of energy for both $a^{(1)}$ and $a^{(2)}$, with a more defined peak at $St \approx 10^{-1}$ for $a^{(2)}$. As a measure of the important role of low frequencies we can observe that 62% and 63% of the energy of the mode for the first and second coefficients, respectively, are contained for Strouhal values less than 10^{-1}.

5. On-road results

The response of the wake of the vehicle to on-road perturbations of the velocity seen by the vehicle is analysed in this section. We conducted numerous tests and a subset is shown in Table 1. The two on-road tests presented hereafter are the two test cases highlighted in bold in the Table. These two tests provide a comprehensive overview of the wake behavior under different conditions, allowing us to draw meaningful conclusions about the vehicle's wake behaviour when compared to wind tunnel tests at zero yaw angle. The robustness of these results is discussed in detail in Cembalo [42]. As shown in Table 1, the conclusions discussed below apply to all on-road tests with only minor differences on energy content in the POD decomposition or spectral energy density of the temporal coefficients.

In Figure 6 (a), the results are from a test on the La Ferté-Vidame track, while in part (b), it corresponds to a test on the RDE-like route. Atmospheric pressure information as well as wind speed and orientation for the two tests are detailed in Table 1.

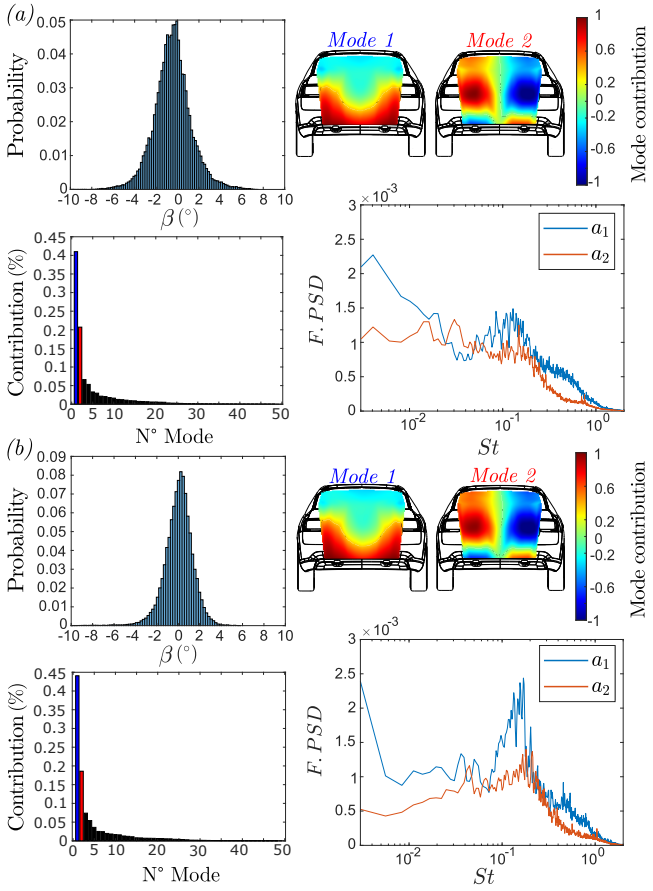

Figure 6: Results of wake analysis on track and on the RDE-like route. Presentation of the distribution of β, the first two modes, and the percentage contribution to the total energy as well as spectral analysis of the temporal coefficients associated with the two modes. (a) Results for test 08 on August 6, 2021, at the La Ferté-Vidame track. (b) Results for test 04 on July 22, 2021, on the RDE-like route.

Regarding the test conducted at La Ferté-Vidame, the direction of travel was counterclockwise, as indicated by the red triangles in Figure 2. The test route includes approximately 4 laps on the Outer track and 2 laps on the Bel Air track. There is very little traffic on this road closed to public. When compared to RDE test conditions, the surroundings of the road on the Stellantis track is repeated at

Routes	$V_{wind}[km/h]$	O_{wind}	$P_{atm}[hPa]$	$\mu_\beta\,[^\circ]$	$\sigma_\beta\,[^\circ]$	% $(\Phi_1+\Phi_2)$	% a_1/a_2 $(St \leq 10^{-1})$	ξ/ξ_0
Track	**22**	**North-West**	**975**	**-0.45**	**1.74**	**62**	**79 and 79**	**3.01**
Track	25	South-West	975	-0.19	1.68	62	79 and 79	5.52
Track	13	South	974	-0.44	1.52	63	78 and 79	3.57
Outer-Track	14	South	979	0.02	1.37	56	76 and 81	2.71
Track	16	South-West	978	-0.08	1.54	63	77 and 79	2.79
Track	8	South	987	-0.31	1.04	69	74 and 69	3.01
Outer-Track	3	South-Est	988	-0.34	1.24	56	75 and 78	2.3
Outer-Track	6	Est	987	0.01	1.15	58	77 and 77	2.43
Outer-Track	6	North-Est	987	0	1.10	55	75 and 77	2.24
RDE-like	8	South-West	1021	-0.02	1.23	55	79 and 70	3.26
RDE-like	**9**	**South-Est**	**1021**	**-0.02**	**1.07**	**63**	**81 and 70**	**3.66**
RDE-like	12	North-Est	1015	-0.54	1.56	57	76 and 67	2.84
Highway	12	North-Est	1015	-0.18	1.63	53	72 and 72	1.98
RDE-like	21	North	1009	-0.18	1.65	55	76 and 72	3.66
RDE-like	25	North-Est	1009	0.1	1.4	55	76 and 70	3.03
RDE-like	3	South-West	1022	0.02	1.41	63	72 and 65	6.22
RDE-like	6	West	1021	0.1	1.54	60	69 and 69	2.85

Table 1: Some statistics to show the robustness of the on-road tests. Hereafter, the two tests in bold will be analysed in detail.

each lap while it displays more diversity on public roads.

It is interesting to note that the distributions of β are very different to that observed in Figure 5. On the track (part (a) of the Figure 6), the distribution has a mean $\mu_\beta = -0.45^\circ$ and a standard deviation $\sigma_\beta = 1.74^\circ$, while on the RDE-like route (part (b) of the Figure 6), the distribution has a mean $\mu_\beta = -0.02^\circ$ and a standard deviation $\sigma_\beta = 1.07^\circ$. On the track, the distribution is not centered at $\beta = 0^\circ$, which is consistent with the counterclockwise direction of the laps. Additionally, the wind speed was higher during the track test, which may explain the difference observed in the standard deviation.

POD modes 1 and 2 have a very clear large scale signature corresponding to respectively vertical and horizontal balance of the wake. They are very similar for both on-road tests. They are also qualitatively similar to the main POD modes obtained in the wind tunnel at zero yaw angle. However, some details differ, for example the signature of mode 2 at the bottom part of the base. The contribution of these two modes to the total energy is now 63%. This is a very significant increase when compared to the wind tunnel tests (45% contribution for these two modes).

On the RDE-like route, a slight increase in the energy contained in mode 1 (about 44%) and a slight decrease in mode 2 (about 19%) is observed. However, the sum of the energy contained in the two modes remains almost unchanged. Looking now at the premultiplied spectra of the temporal coefficients associated to modes 1 and 2, an increase of the energy in the low frequency domain is observed for the first mode. For all these tests, 70% to 80% of the energy content is measured for Strouhal numbers lower than 0.1. Note that, for on-road situations, the vehicle velocity V used in the computation of the Strouhal number in figure 6 is the average vehicle velocity during the test.

A higher frequency resolution ($\Delta f = 5.10^{-3}\ Hz$) was obtained by using longer blocks and therefore a lower number of blocks for averaging the spectra ($N_{blocks} \leq 13$). The results are presented in Figure 7. The presence of a large band contribution for Strouhal numbers lower than 10^{-2} is very clear, especially for the first mode corresponding to the vertical wake balance (Figure 6). We observe that very low frequencies (down to $St \approx 10^{-3}$) contribute to the power spectrum. At the average speed maintained during the track test, the distance traveled by the car during a period $T = 1/f$ can be estimated as $d \approx V.T = H/St$ which is very large for Strouhal numbers lower than 10^{-2}. We stress that a quasi steady response of the wake is expected for these low Strouhal numbers. This is an important aspect because these low frequencies do not only come from wind turbulence. They probably also originate from the variation in the flow seen by the car due to a variable environment having a wide range of longitudinal scales along the road. Indeed, driving along road portions having similar characteristics (freely exposed to side winds, protected in a forest, exposed to urban area features, ...) will induce low frequency components corresponding to the time taken to travel along these portions. Of course, sharp changes in wind directions occur while entering to - or emerging from - a sheltered portion. However, careful experimental study by Haffner et al. [41] using a model geometry at reduced scale shows that natural or provoked wake switching between right/left asymmetry is a slow process taking place in approximately 30 convective time scales. This corresponds to $St \approx 1/30$. The slow reorganisation of the large scale wake therefore acts as a low-pass filter that cuts high frequency disturbances.

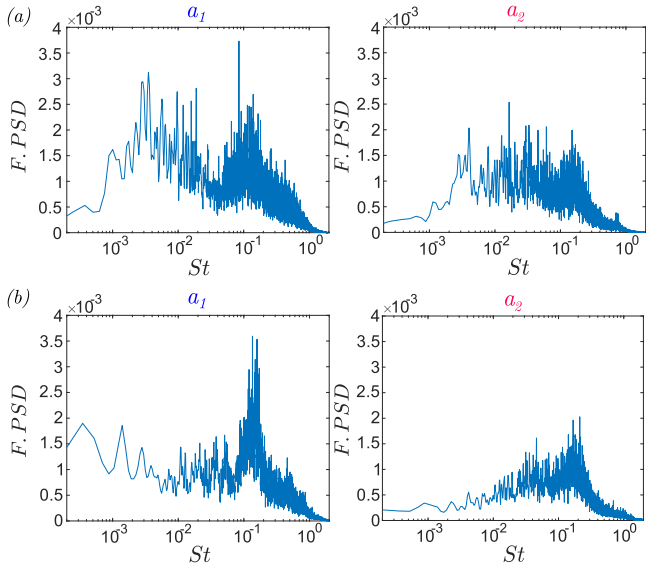

Figure 7: Results of the spectral analysis of the temporal coefficients with a frequency resolution of $\Delta f = 5.10^{-3}[Hz]$ for the track and RDE-like route tests. (a) Coefficients $a^{(1)}$ and $a^{(2)}$ on the track. (b) Coefficients $a^{(1)}$ and $a^{(2)}$ on the RDE-like route.

6. Statistical analysis at varying yaw angle in the wind tunnel

Going back to the wind tunnel, we can try to reproduce the yaw angle distribution observed on the road. A subset of yaw angles of the vehicle is first chosen. One single continuous wind tunnel test of approximately 20 minutes - the total number of sample is 120687 at a sampling rate of 100 Hz - is used for the test shown in Figure 8. During the test, our choice is to impose a variable measurement time for each vehicle yaw angle of the subset in order to have a data set representative of the statistical distribution of yaw angles observed on the road.

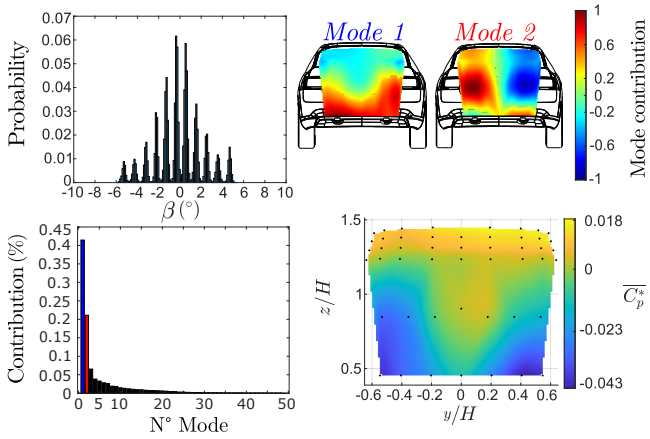

Figure 8: Results of the wake analysis for a varying yaw angle in the wind tunnel. Presentation of the distribution of β, the first two modes and the percentage of their contribution to the total energy. The time averaged value $\overline{C_p^*(\mathbf{x},t)}$ at the base for the full test is shown on bottom right plot

Modes 1 and 2 are very similar to on road modes. We observe that nearly 63% of the turbulent kinetic energy is contained in the first two modes. This is also very similar to the energy distribution for on-road tests. Moreover, the energy contained in the first mode has almost doubled compared to the static yaw angle test, which seems to be due to the variation of the yaw angle along the tests, similarly to what we could observe on the road. This is a good indication of the interest for making these quasi steady tests during vehicle development to test the robustness of a vehicle design to yaw angle perturbations.

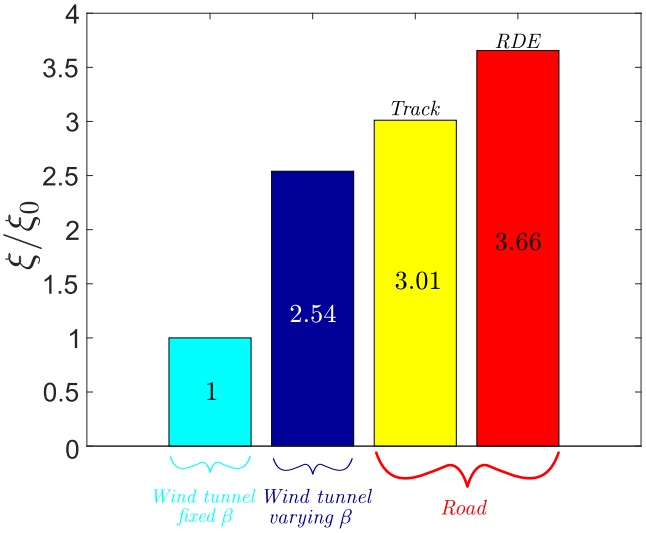

Figure 9: Comparison of total variance ξ for the different tests considered. In sky blue, the wind tunnel case with fixed β. In dark blue, the wind tunnel case with varying β. In yellow and red, the cases on track and on the RDE-like route respectively.

The total energy ξ measured in the different tests is compared in Figure 9 to that measured in the wind tunnel for a fixed yaw angle. This ratio increases significantly for the test with dynamic variation of β in the wind tunnel, reaching more than double the reference value ($\xi/\xi_0 \approx 2.5$). The total energy further increases on the road. On the track, the difference is similar to the cases with dynamically varying β in the wind tunnel ($\xi/\xi_0 \approx 3.01$), while on the RDE-like route, the total variance increases even more ($\xi/\xi_0 \approx 3.66$) compared to the value observed in the wind tunnel for fixed yaw, which is a very significant difference.

The imposed quasi static variations of the yaw angle are interesting in order to widen the statistical distribution of the projection of instantaneous pressure footprints on the main POD modes that represent the wake vertical and horizontal asymmetries. These modes are very similar to on-road main modes and this is an interesting property for wind tunnel tests to be confirmed on other vehicle geometries.

Figure 10 shows the distribution of the first and second temporal coefficients as function of the yaw angle. Each group corresponds to a prescribed orientation of the vehicle during the dynamic tests. The red dot is the conditional average of the temporal coefficient for each orienta-

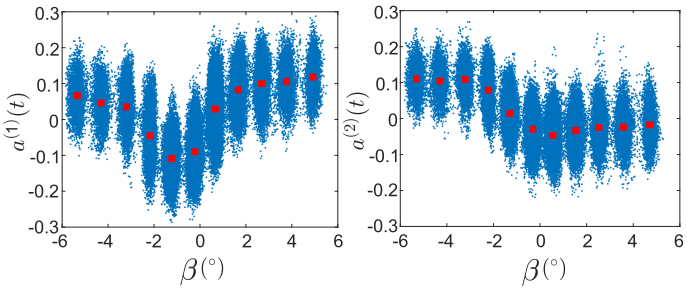

Figure 10: Distribution of the temporal coefficients $a^{(1)}$ and $a^{(2)}$ as function of the yaw angle β in the varying yaw angle test. The red dot is the conditional average of the temporal coefficient for each orientation of the vehicle.

tion of the vehicle. We see that the POD decomposition is able to describe a large span of wake states at the base. It is well known that drag increases with yaw angle. For the largest positive or negative yaw angles considered here, the change of sign of $a^{(2)}$ corresponds to a change in left/right asymmetry. As $a^{(1)}$ is concerned, we see that positive values correspond to large yaw angles while small yaw angles - and therefore minimum drag - are associated statistically to negative values of $a^{(1)}$. The time averaged value $\overline{C_p^*(\mathbf{x},t)}$ at the base for the full test is also shown in Figure 8. This mean distribution displays approximately a left/right symmetry and a positive pressure gradient (pressure increases when moving upward). Using the POD decomposition a low order representation of $C_p^*(\mathbf{x},t)$ can be obtained using the first two modes only. From the signature of the mean distribution, from the spatial distribution of the two dominant modes shown in Figure 8 and from the conditional values of the temporal coefficients discussed above, it is easy to figure out that the wake is evolving from a positive vertical asymmetry at about zero yaw to a horizontal asymmetry at larger yaw. Indeed, at larger yaw, a positive value of $a^{(1)}$ reduces the vertical gradient while a non zero $a^{(2)}$ corresponds to horizontal pressure gradients. Considering the similarities with on-road results, we therefore conclude that a low frequency exploration of such wake large scale states is performed during on-road travel. Therefore, even a quasi-steady closed loop control able to maintain a prescribed wake balance would be interesting for drag reduction. This approach is proposed for a reduced scale model using actuated flaps located at the back of a model vehicle in Cembalo [42] and Cembalo et al. [28].

7. Key findings and Conclusions

Under disturbed upstream conditions, the near wake region of a vehicle loses its average symetry, resulting in an increase of drag. The aim of this research work was to analyse the effect of on-road perturbations on the asymmetry of a vehicle wake with two major questions, (1) to determine if the external perturbations seen by the vehicle result in significant vertical or horizontal large-scale asymmetries of the wake, (2) to see if low frequency global wake motions have a major contribution in real situations. We described the vehicle used for testing in a full-scale wind tunnel, on a track and on a RDE-like route. Additionally, we detailed the measurement systems and experimental setup. To analyze the wake characteristics in the wind tunnel and on the road, Proper Orthogonal Decomposition (POD) of the pressure distribution on the base of the vehicle was employed. The main results are summarized below:

- Wind tunnel tests with fixed yaw substantially deviate from road conditions, showing lower modal energy content and different wake modal footprints, yet still corresponding to similar large scale vertical or horizontal wake asymmetries. The low-frequency energy content of the temporal coefficients of the mode is very different from that observed on-road.

- Road tests exhibit a nearly normal distribution of yaw angle, with values consistently between $\pm 10°$ and $-5° \leq \beta \leq 5°$ for over 95% of the time. POD analysis also reveals two primary modes, associated with vertical and horizontal wake asymmetries, respectively. More than 60% of the total energy is carried by these two modes. Low frequencies (even very low ones down to $St \approx 10^{-3}$) play a major role, corresponding to a quasi-static perturbation domain. Indeed, over 70% of the energy of the two main modes is contained within frequencies $St \leq 10^{-1}$;

- A wind tunnel run can be designed by selecting a subset of vehicle yaw and a variable measurement time for each yaw. The large data set obtained is then representative of the statistical distribution of yaw angles observed on the road. This single run captures phenomena similar to those observed on the road. The footprint of the two main modes are very similar. The energy content in the first two modes is higher and closer to that measured on road. These tests also show that multiple large scale wake states contribute to the first two modes. Considering the similarities with on-road results, we conclude that a low frequency large span exploration of such wake states is performed during on-road travel.

Further studies should complete this analysis. It would be interesting to analyse the effect of pitch angle variations on these large scale modes. Moreover, the tests have been conducted on a single vehicle. It would be interesting to see the robustness of these results on other types of vehicle. We also stress that a quasi steady response of the wake is expected for the energy containing low Strouhal numbers observed on the road. Therefore, the use of steady CFD computations for a subset of yaw angles is interesting to evaluate a vehicle on-road characteristics. Moreover, even a quasi-steady closed loop control able to maintain a prescribed wake balance would be promising for drag reduc-

tion strategies. With this perspective in mind, a quasi-steady closed loop control able to maintain a prescribed wake balance on a 2/5 reduced scale Windsor model was recently proposed by Cembalo et al. [28] using recursive subspace-based predictive control.

Acknowledgements

The authors would like to warmly thank Sylvain Aguinaga for insighful discussions, Jean Charles Boueilh for invaluable support during the experiments, as well as Yann Goraguer for moral and technical assistance.

Funding

This research project was funded by STELLANTIS and Ministry for Higher Education and Research. Agostino Cembalo wishes to acknowledge support from ANRT PhD scholarship.

Competing interest

The authors report no conflict of interest.

References

[1] G. Kadijk and N. Ligterink. Road load determination of passenger cars. *TNO Report: TNO*, 2012.

[2] W. H. Hucho and G. Sovran. Aerodynamics of road vehicles. *Ann. Rev. Fluid. Mech.*, 25:485–537, 1993.

[3] R. K. Cooper. Atmospheric turbulence with respect to moving ground vehicles. *J. Wind Eng. Ind. Aerodyn.*, 17, 1984.

[4] S. Watkins, J. W. Saunders, and P. H. Hoffmann. Turbulence experienced by moving vehicles. part i. introduction and turbulence intensity. *J. Wind Eng. Ind. Aerodyn.*, 57:17, 1995.

[5] G. Carlino, D. Cardano, and A. Cogotti. A new technique to measure the aerodynamic response of passenger cars by a continuous flow yawing. *SAE Technical papers*, 0148-7191:16, 2007. doi: https://doi.org/10.4271/2007-01-0902.

[6] J. Garcia de la Cruz, R. Brackston, and J. Morrison. Adaptive base-flaps under variable cross-wind. *SAE Technical Papers*, 2017. doi: 10.4271/2017-01-7000.

[7] T. Yamashita, T. Makihara, K. Maeda, and K. Tadakuma. Unsteady aerodynamic response of a vehicle by natural wind generator of a full-scale wind tunnel. *SAE International Journal of Passenger Cars - Mechanical Systems*, pages 358 – 368, 2017.

[8] D. Stoll and J. Wiedemann. Active crosswind generation and its effect on the unsteady aerodynamic vehicle properties determined in an open jet wind tunnel. *SAE Technical Paper*, 11(2018-01-0722), 2018. doi: https://doi.org/10.4271/2018-01-0722.

[9] J. Howell, D. Forbes, and M. Passmore. A drag coefficient for application to the wltp driving cycle. *Proceedings of the Institution of Mechanical Engineers, Part D: Journal of Automobile Engineering*, 231(9):1274–1286, 2017. doi: 10.1177/0954407017704784.

[10] U.N. Global Technical Regulations. Proposal for a new global technical regulation on the worldwide harmonized light vehicles test procedure (wltp). *World Forum for Harmonization of Vehicle Regulations*, 2014.

[11] S. McTavish and B. McAuliffe. Improved aerodynamic fuel savings predictions for heavy-duty vehicles using route-specific wind simulations. *J. Wind Eng. Ind. Aerodyn.*, 210, 2021. doi: https://doi.org/10.1016/j.jweia.2021.104528.

[12] C. Brown, D. Burton, T. Crouch, and M. C. Thompson. The influence of turbulence on cycling aerodynamics,. *J. Wind Eng. Ind. Aerodyn.*, 242, 2023. doi: https://doi.org/10.1016/j.jweia.2023.105575.

[13] K. Cooper and S. Watkins. The unsteady wind environment of road vehicles, part one: A review of the on-road turbulent wind environment. *SAE Technical Paper*, 2007-01-1236:20, 2007. doi: https://doi.org/10.4271/2007-01-1236.

[14] S. Watkins and K. Cooper. The unsteady wind environment of road vehicles, part two: Effects on vehicle development and simulation of turbulence. *SAE Technical Paper*, 2007-01-1237: 17, 2007. doi: https://doi.org/10.4271/2007-01-1237.

[15] P. Hu, Y. Han, C. S. Cai, W. Cheng, and W. Lin. New analytical models for power spectral density and coherence function of wind turbulence relative to a moving vehicle under crosswinds. *J. Wind Eng. Ind. Aerodyn.*, 188, 2019. doi: https://doi.org/10.1016/j.jweia.2019.02.005.

[16] Y. Su, M. Li, Y. Yang, J. Mann, H. Liao, and X. Li. Experimental investigation of turbulent fluctuation characteristics observed at a moving point under crossflows. *J. Wind Eng. Ind. Aerodyn.*, 197, 2020. doi: https://doi.org/10.1016/j.jweia.2019.104079.

[17] S. Wordley and J. Saunders. On-road turbulence. *SAE International Journal of Passenger Cars: Electronic and Electrical Systems*, 1(1):341–360, 2008. ISSN 1946-4614.

[18] S. Wordley and J. Saunders. On-road turbulence: Part 2. *SAE International Journal of Passenger Cars: Mechanical Systems*, 2(1):111–137, 2009. ISSN 1946-3995. doi: 10.4271/2009-01-0002.

[19] D. Schröck, N. Widdecke, and J. Wiedemann. On-road wind conditions experienced by a moving vehicle. In *FKFS-Konferenz—Progress in Vehicle Aerodynamics, Stuttgart*, 2007.

[20] G. Bonnavion, O. Cadot, V. Herbert, S. Parpais, R. Vigneron, and J. Délery. Asymmetry and global instability of real minivans' wake. *J. Wind Eng. Ind. Aerodyn.*, 184, 2019. doi: https://doi.org/10.1016/j.jweia.2018.11.006.

[21] M. Rüttgers, J. Park, and D. You. Large-eddy simulation of turbulent flow over the drivaer fastback vehicle model. *J. Wind Eng. Ind. Aerodyn.*, 186, 2019. doi: https://doi.org/10.1016/j.jweia.2019.01.003.

[22] D. Burton, S. Wang, D. Tudball Smith, H. N. Scott, T. N. Crouch, and M. C. Thompson. The influence of background turbulence on ahmed-body wake bistability. *J. Fluid Mech*, 926, 2021. doi: http://dx.doi.org/10.1017/jfm.2021.706.

[23] M. Urquhart and S. Sebben. Optimisation of trailing edge flaps on the base cavity of a vehicle for improved performance at yaw. *Flow, Turbulence and Combustion*, 109, 2022. doi: 10.1007/s10494-022-00323-z.

[24] M. Urquhart, M. Varney, S. Sebben, and M. Passmore. Drag reduction mechanisms on a generic square-back vehicle using an optimised yaw-insensitive base cavity. *Experiments in Fluids*, 62, 2021. ISSN 1432-1114. doi: 10.1007/s00348-021-03334-0.

[25] A. K. Perry, M. Passmore, and G. Pavia. Influence of short rear end tapers on the wake of a simplified square-back vehicle: wake topology and rear drag. *Experiments in Fluids*, 57, 2016. doi: https://doi.org/10.1007/s00348-016-2260-3.

[26] M. Varney, M. Passmore, and A. Gaylard. Parametric study of asymmetric side tapering in constant cross wind conditions. *SAE Tech. Report. No. 2018-01-0718, Society of Automotive Engineers*, 2018. doi: https://doi.org/10.4271/2018-01-0718.

[27] R. Li, J. Borée, B.R. Noack, L. Cordier, and F. Harambat. Drag reduction mechanisms of a car model at moderate yaw by bi-frequency forcing. *Phys. Rev. Fluids*, 4(034604), 2019.

[28] A. Cembalo, P. Coirault, J. Borée, C. Dumand, and G. Mercère. Active control of road vehicle's drag for varying upstream flow conditions using a recursive subspace based predictive control methodology. *Control Engineering Practice*, 152:106071, 2024. ISSN 0967-0661. doi: https://doi.org/10.1016/j.conengprac.2024.106071.

[29] M. Stellato and L. Betti. Fca full scale wind tunnel: Wltp and coast down test performed with wind tunnel method.

SAE Technical Paper, 37(2018-37-0017), 2018. doi: 10.4271/2018-37-0017.

[30] D. Clavaud. Actions du vent sur les bâtiments selon l'eurocode 1 –partie 1-4. *Techniques de l'ingénieur Ref C3306*, 2014.

[31] Technical Committee CEN/TC250. Eurocode 1 : actions on structures. part 1-4 general actions – wind actions. *AFNOR*, pages 1–48, 2005.

[32] S.H. Chue. Pressure probes for fluid measurement. *Progress in Aerospace Sciences*, 16(2):147–223, 1975. ISSN 0376-0421. doi: https://doi.org/10.1016/0376-0421(75)90014-7.

[33] L. Thomann. Mesures aérodynamiques en environnement réel. Technical report, Polytech Tours, 2018.

[34] A. Gravier. Correction de l'influence des tubes sur la mesure de pression instationnaire. Technical report, ISAE-SUPAERO, 2023.

[35] H. Tijdeman and H. Bergh. Theoretical and experimental results for the dynamic response of pressure measuring systems. Technical report, NATIONAL AERO AND ASTRONAUTICAL RESEARCH INSTITUT AMSTERDAM, 1965.

[36] J. L. Lumley. The structure of inhomogeneous turbulent flows. *Atmospheric turbulence and radio wave propagation*, pages 166–178, 1967.

[37] A. Chatterjee. An introduction to the proper orthogonal decomposition. *Current Science*, 78(7):808–817, 2000. ISSN 00113891. URL `http://www.jstor.org/stable/24103957`.

[38] L. Cordier and M. Bergmann. Proper Orthogonal Decomposition: an overview. In *Lecture series 2002-04, 2003-03 and 2008-01 on post-processing of experimental and numerical data, Von Karman Institute for Fluid Dynamics, 2008.*, pages 1 – 46. VKI, 2008. URL `https://hal.science/hal-00417819`.

[39] K. Taira, S.L. Brunton, S.T.M. Dawson, C. W. Rowley, T. Colonius, B.J. McKeon, O.T. Schmidt, S. Gordeyev, V. Theofilis, and L.S. Ukeiley. Modal analysis of fluid flows: An overview. *AIAA Journal*, 55(12):4013 – 4041, 2017. doi: 10.2514/1.J056060.

[40] J. Weiss. A tutorial on the proper orthogonal decomposition. *American Institute of Aeronautics and Astonautics*, pages 1–21, 2019. doi: https://doi.org/10.2514/6.2019-3333.

[41] Y. Haffner, J. Borée, A. Spohn, and T. Castelain. Mechanics of bluff body drag reduction during transient near wake reversals. *J. Fluid Mech.*, 894:A14, 2020.

[42] A. Cembalo. *Stratégie innovante d'optimisation de la traînée aérodynamique en temps réel pour l'amélioration de l'efficacité énergétique des voitures.* PhD thesis, École Nationale Supérieure de Mécanique et d'Aérotechnique, 2024.